powders

MDPI

Article

Effects of Process Parameters on Cold Spray Additive Manufacturing of Quasicrystalline $Al_{93}Fe_3Cr_2Ti_2$ Alloy

Aylanna Priscila Marques de Araujo [1,*], Felipe B. Do M. Carmelo [2], Erlifas M. Rocha [1], Claudio S. Kiminami [1,2] and Piter Gargarella [1,2,3]

[1] Graduate Program in Materials Science and Engineering, Federal University of São Carlos, Rod. Washington Luis Km 235, São Carlos 13565-905, SP, Brazil; erlifas@estudante.ufscar.br (E.M.R.); kiminami@ufscar.br (C.S.K.); piter@ufscar.br (P.G.)
[2] Department of Materials Engineering (DEMa), Federal University of São Carlos (UFSCar), Rod. Washington Luis Km 235, São Carlos 13565-905, SP, Brazil; felipebiasimontecarmelo@estudante.ufscar.br
[3] Center for Characterization and Development of Materials (CCDM), Federal University of São Carlos (UFSCar), Rod. Washington Luiz, Km 235, São Carlos 13565-905, SP, Brazil
* Correspondence: aylanna@estudante.ufscar.br or aylannapriscila@hotmail.com

Abstract: Quasicrystalline $Al_{93}Fe_3Cr_2Ti_2$ (at.%) gas-atomized powders, which exhibit a metastable composite microstructure, were used to produce coatings by cold spray additive manufacturing processing (CSAM) using different processing parameters. The metastable composite microstructure provides the $Al_{93}Fe_3Cr_2Ti_2$ alloy with excellent mechanical properties. At the same time, the metastability of its microstructure, achieved by the high cooling rates of the gas atomization process, limits the processability of the $Al_{93}Fe_3Cr_2Ti_2$ powder. The purpose of this study was to investigate the effect of process parameters on the CSAM of quasicrystalline $Al_{93}Fe_3Cr_2Ti_2$ powder. The powder was sieved and classified to a size range of −75 µm. Using N_2 carrier gas combined with different temperatures, pressures, nozzle apertures, and deposition substrate conditions, cold-sprayed coatings were produced. The porosity and thickness of the coatings were evaluated by image analyses. By SEM, XRD, DSC, and TEM, the microstructure was identified, and by Vickers microhardness, the mechanical properties of the coatings were investigated. Dense (≤0.50% porosity) and thick (~185.0 µm) coatings were obtained when the highest pressure (4.8 MPa), highest temperature (475 °C), and lowest nozzle aperture (A) were used in combination with an unblasted substrate. The SEM, XRD, and DSC data showed that the composite powder's microstructure was retained in all coatings with no decomposition of the metastable i-phase into equilibrium crystalline phases. Supporting these microstructural results, all coatings presented a high and similar hardness of about 267 ± 8 HV. This study suggests that the CSAM process could, therefore. produce metastable quasicrystalline $Al_{93}Fe_3Cr_2Ti_2$ coatings with a composite microstructure and high hardness.

Keywords: Al-based quasicrystalline alloys; cold spray additive manufacturing (CSAM) processing; process parameters; microstructure and mechanical properties of coatings

Citation: de Araujo, A.P.M.; Carmelo, F.B.D.M.; Rocha, E.M.; Kiminami, C.S.; Gargarella, P. Effects of Process Parameters on Cold Spray Additive Manufacturing of Quasicrystalline $Al_{93}Fe_3Cr_2Ti_2$ Alloy. *Powders* **2023**, *2*, 525–539. https://doi.org/10.3390/powders2030033

Academic Editor: Nikolay Z. Lyakhov

Received: 31 March 2023
Revised: 9 June 2023
Accepted: 3 July 2023
Published: 14 July 2023

1. Introduction

Cold-Spray Additive Manufacturing (CSAM) processing is a unique technique that relies on the acceleration of metallic powder through a nozzle using high-pressure, preheated propellant gas (air, helium, or nitrogen gas) at supersonic rates (300–1500 (m/s)) to produce deposits onto a substrate [1,2]. Once the particles strongly collide with a substrate (also called base material), they are plastically deformed and continuously deposited, forming a layer-by-layer cold-sprayed part [1–3]. Because of the high impact of the powder feedstock, severe plastic deformation occurs at the interface of substrate/particles or pre-deposited particles/particles. Consequently, the mechanical interlocking of metallic particles promotes metallurgical bonding [4]. Compared to other additive manufacturing (AM) processes, such as the Powder Bed Fusion (PBF) process, the main advantage of CSAM is that the working temperature of the feedstock powder remains far below its melting point during the entire process. Thus, with the inclusion of impurities, oxidation, the evaporation of elements, gas release, phase transformation, residual thermal stresses, and other adverse effects (introduced by high temperature) are avoided [5,6]. In addition to its high processing flexibility, the unlimited size possibilities to be manufactured, and the capacity to repair damaged products, CSAM is well-suited to highly reflective materials such as copper and aluminum-based alloys [3]. Both materials quickly dissipate heat and are not easily melted by the laser source energy commonly used in other AM processes. However, the properties of cold-sprayed parts, such as density, porosity, adhesion, thickness, microstructure, and hardness, depend on the deposition parameters. For example, in order to produce good cold-sprayed parts, the deposition parameters have to be set to spray particles in a specific velocity range or deposition window [6] and on a substrate with an appropriate finishing surface [3].

CSAM for high-strength aluminum-based alloys has started with corrosion-resistant coatings, and the repairing of aeronautics and aerospace parts [2]. The literature has reported that cold-sprayed Al6061 deposits have improved in their corrosion resistance with heat treatment, independently of the building direction [7]. For the Al7075 alloy, authors [2,8,9] searched to improve the deposition efficiency by using the preheating treatment of powder feedstock. In these cases, the researchers claimed the poor deposition ability of the as-produced powder, which was due to the presence of very fine precipitates and high hardness. Thus, by heating-treating the Al7075 powders, their microstructure became coarser, improving the deposition efficiency during the Cold-Spray (CS) processing. Other well-known classes of high-strength aluminum-based alloys are those that are able to form quasicrystalline phases: so-called quasicrystalline (QC) alloys. Aluminum-based QC alloys have been developed with microstructures of nano to micrometer-sized QC particles embedded in an α-Al matrix [10–13]. Due to its hard and brittle characteristics at room temperature, the dislocation movement through the quasiperiodic lattice of the QC phase is very difficult [14,15]. However, when combined with a ductile metallic matrix, the QC phases are excellent reinforcements [14,16–20]. Nevertheless, the precipitation of the QC phases in a matrix requires high cooling rates (~10^3–10^6 K/s) [21,22] during the solidification process. It justifies Aluminum-based QC alloys that are conventionally processed by rapid solidification processes such as melt spinning [12], copper mold suction casting [23], laser surface remelting [20,22], and gas atomization [24,25] with subsequent consolidation via hot extrusion [26]. Preliminary studies on the CSAM processing of the quasicrystalline former Al-Cr-Mn-Co-Zr alloy were conducted by the authors [27]. They reported that composite coatings 180 μm thick, with a porosity lower than 1%, and an interface free of cracks or detachments were obtained using He as a carrier gas, with a gun temperature and pressure of 430 °C and 3.5 MPa, respectively. The presence of the icosahedral quasicrystalline phase was evident as a consequence of the low working temperature of the CS process, and a hardness of 301 ± 25 HV was achieved [27]. According to the literature, the Al-Fe-Cr-Ti quasicrystalline former alloy presented with high thermal stability at its i-QC phase (430 °C) combined with distinguished hardness and tensile strength at a temperature range from room temperature to 350 °C [12,28]. Due to the low solubility and the atomic diffusivity of Cr, Fe, and Ti in aluminum, when the Al–Fe–Cr–Ti system was submitted to high cooling rates, the solubility of the α-Al phase increased and the formation of metastable phases was favored [12,23]. However, the metastability of the i-QC phase became a concern in the processing of this alloy once it could be decomposed into its approximants phases or a stable crystalline phase, as reported [12,15,28,29]. Recently, our research group identified that it was possible to use recycled aluminum cans to produce quasicrystalline phase former Al-Fe-Cr-Ti alloys through gas atomization, where metastable quasicrystals with high thermal stability (~500 °C) were precipitated [30]. Thus, for researchers and industries, it would be necessary and valuable to understand the behavior of the Al-Fe-Cr-Ti gas when atomized and submitted to a promising and challenging process, such as CSAM.

In the present study, the effects of the processing parameters on the CSAM of the quasicrystalline $Al_{93}Fe_3Cr_2Ti_2$ alloy were investigated. The porosity, adherence, thickness, roughness, microstructure, and Vickers microhardness of the $Al_{93}Fe_3Cr_2Ti_2$ cold-sprayed coatings were evaluated. Based on the results of the analyses, it was concluded that the alloy studied could be produced by CSAM with less than 0.50% porosity while being well adhered to the substrate and presenting a composite microstructure with the metastable i-phase retained and high hardness (267 ± 8 HV).

2. Materials and Methods

2.1. Coatings Preparation

The composite powder used in these cold spray additive manufacturing (CSAM) trials was the same as that used to produce the bulk parts by the selective laser melting (SLM) processing for the previous studies [30]. The ingots, with the nominal chemical composition of $Al_{93}Fe_3Cr_2Ti_2$ (at.%), were gas atomized (PSI Hermiga 75/5VI) using argon with 40 bar of pressure and a gas-to-melt mass flow ratio (GMR) of 3. The details of the powder production and its characterization are presented in [30]. The powder sieved −75 µm of mesh, the size distribution of which is presented in Figure 1a, and a microstructure is shown in Figure 1b.

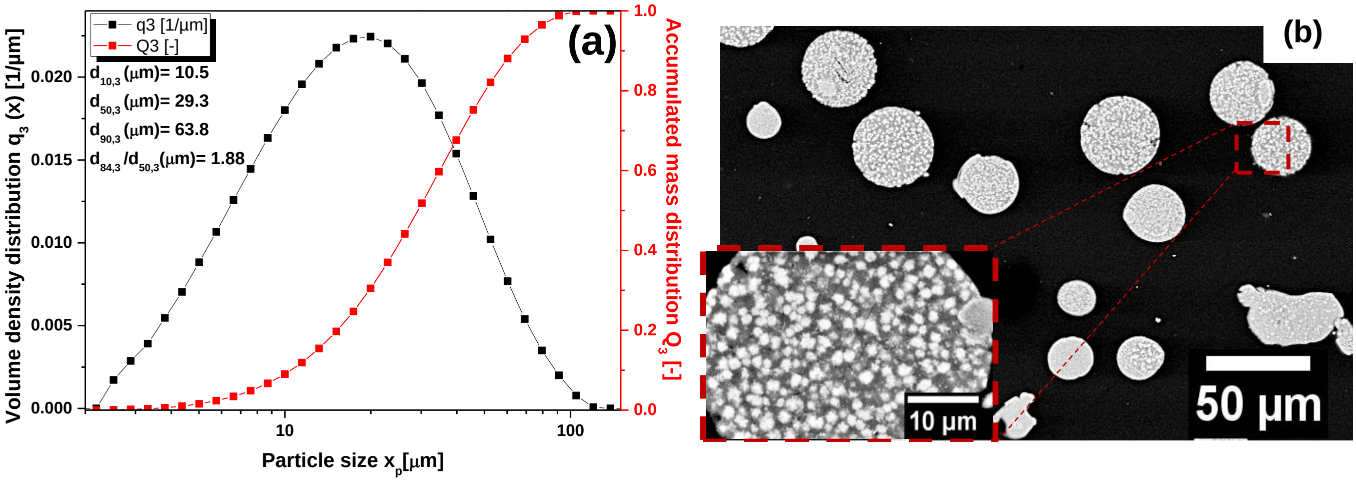

Figure 1. (**a**) Particle size distribution of the gas-atomized $Al_{93}Fe_3Cr_2Ti_2$ powder (−75 µm) and (**b**) SEM (Backscattered Electron (BSE) mode) micrographs of powder's cross-section. The insert image shows the details of the powder's microstructure in higher magnification.

Before spraying, the powder was heated in a vacuum at 125 °C to drive off any adsorbed moisture. The cold spray additive manufacturing (CSAM) apparatus used in this study was a PCS-100 (Plasma Giken, Saitama, Japan) cold spray system with a high-pressure system designed and built at Polycontrols Technologies corporation with a powder preheating/mixing chamber prior to the throat of the nozzle. The throat nozzle of the equipment is made of polybenzimidazole (PBI) polymer. For the experiments, varied parameters were used, as shown in Table 1, and for all of them, nitrogen was used as a carrier gas. Because the velocity of the powder particles (PV) depended on the pressure and temperature of the N_2 carrier gas for each experiment, PV was measured using an accuraspray 4.0 device, and its values are presented in Table 1. Two nozzle apertures were used in this work, a lower one named "A" and a higher one named "B". Due to the confidentiality of the company, it was not possible to provide the exact values of the nozzle aperture used in this work. The deposition was performed onto Al 6061 substrates in the T6 condition. For three of these experiments, immediately prior to depositing the coatings, the substrate's surfaces were manually prepared using sandblasting with a SiC grit #24 and compressed air at 60 psi. The visual aspect of the coatings prepared in different substrate conditions is shown in Figure 2.

Table 1. Varied parameters for conducted cold spray additive manufacturing experiments. Legend: P: pressure, T: temperature, NA: nozzle aperture, PV: particles' velocity, and AB: abrasive blasting of the substrate.

Coating ID	P (MPa)	T (°C)	NA (mm)	PV (m/s)	AB
1	4.0	450	A	600	Yes
2	4.3	450	A	604	Yes
3	4.0	450	A	588	Yes
4	4.8	475	A	610	No
5	4.0	450	B	662	No
6	4.0	475	B	680	No
7	3.4	425	B	630	No

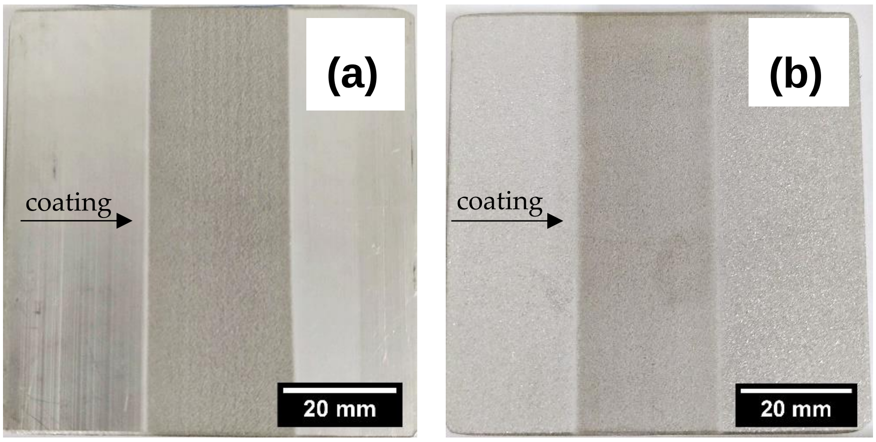

Figure 2. Images of the coatings produced by the CSAM process in an (**a**) unblasted and (**b**) blasted substrate.

2.2. Characterization Methods

For Optical Microscopy (OM), Scanning Electron Microscopy (SEM), and Vickers microhardness (HV), the coating cross-section was cut in the middle and mounted before being ground and polished using conventional metallographic techniques. The samples were not etched, and an Optical Microscopy (OM) Olympus microscope (BX41M-LED) was used to take 18 pictures along the cross-section of the coating using 200× magnification. Using the 18 pictures, the porosity and thickness of the coatings were measured by image analysis using the software ImageJ. For porosity measures, the pores and cracks were quantified for the whole cross-section. For thickness, three measures were performed for each picture (18 × 3 measures for each coating). The roughness of the coatings and substrates was measured using a Mitutoyo SJ-201P rugosimeter, and five measures were executed for each sample. X-ray diffraction (XRD) analyses were performed on a Siemens Model D5005 diffractometer with Cu-Kα radiation, a range of 35–80°, and a step size of 2°/min. For Transmission Electron Microscopy (TEM) analyses, a thin foil of the thicker coating (coating 4) was produced by the conventional method of slicing and grinding, followed by ion-polishing using a Gatan model 691. These studies were carried out in an FEI TECNAI G2 F20 (TEM/Scanning (STEM)) at 200 kV with a field emission gun (FEG) equipped with a multiple energy dispersive X-ray spectroscopy (EDX) detector from EDAX instruments (active area 30 mm^2). The thermal stability was evaluated by Differential Scanning Calorimetry (DSC) using a Netzsch DSC 404 calorimeter with a heating/cooling rate of 40 K/min and with an argon protective atmosphere. Each sample was subjected to two heating cycles to evaluate the presence and stability of quasicrystalline phases. The microstructure of the coatings was investigated using a FEI Scanning Electron Microscopy (SEM) FEI QUANTA 400 model and chemical microanalyses were performed by an energy-dispersive spectrometer (EDS Oxford Instruments, INCAx-sight model), which was attached to the SEM. Vickers microhardness measurements were carried out at the cross-section of the coatings using a FM-800 (Future-Tech). All indents were made at room temperature with a load of 10 gf and a loading time of 15 s. All 18 indents analyzed for each sample were taken at random positions along the whole cross-section.

3. Results and Discussion

3.1. Porosity, Thickness, and Roughness of the Coatings

The coatings produced using different process parameters presented different porosities, adherence, and uniformity. Examples of OM images from cross-sections are shown in Figure 3, and the porosity, thickness and roughness measured are in Table 2. The coatings produced on a blasted substrate (1, 2, and 3) show lower adherence and thickness (of about 48.0 to 85.0 μm) with varying local and worse uniformity, combined with a higher porosity (varying of about 1.50 to 4.17%). Among these three, only coating 2 used a higher pressure of 4.3 MPa and resulted in greater thickness (~85 μm). For the coatings produced on an unblasted substrate (4, 5, 6, and 7), the porosity was lower (0.26 to 0.50%), and the thickness was higher (varying locally from about 88 to 185 μm). Among these four, coating 4, produced with the highest pressure (4.8 MPa), highest temperature (475 °C), and lowest nozzle aperture (A), presented the greatest thickness (185 μm). The thickness variation was due to the undulating coating/substrate interface and the roughness of the coating surface. While the roughness of the blasted substrates was around 6 μm, the roughness of the unblasted ones was about 0.8 μm. This could explain the more undulated interface and lower adherence of the coatings produced on blasted substrates. The coatings' surface roughness varied from 9 μm to 12 μm, and considering the measures deviation, they did not change significantly.

Table 2. Porosity (pores + cracks), thickness, and roughness obtained for the cold-sprayed coatings produced using different process parameters.

Coating ID	Porosity (%)	Thickness (μm)	Coating Roughness (μm)	Substrate Roughness (μm)
1	1.50 ± 0.80	50.0 ± 8.62	9.0 ± 1.43	6.7 ± 1.66
2	1.84 ± 1.32	85.0 ± 7.49	9.8 ± 1.54	5.4 ± 0.30
3	4.17 ± 2.56	48.0 ± 6.72	11 ± 1.60	6.5 ± 1.66
4	0.49 ± 0.25	185.0 ± 22.3	12.2 ± 3.02	0.6 ± 0.08
5	0.26 ± 0.19	95.2 ± 13.96	11.1 ± 2.19	0.5 ± 0.06
6	0.35 ± 0.21	88.0 ± 12.32	12.1 ± 0.69	1.2 ± 0.22
7	0.50 ± 0.21	116.1 ± 18.00	10.5 ± 1.55	0.8 ± 0.41

3.2. Microstructural Analyses

The BSE SEM images of the cold-sprayed coatings produced using different parameters are shown in Figure 4. From these images, the chemical uniformity and phase distribution could be evaluated. The bright contrast of the coatings when compared to the substrate was due to the presence of elements of high atomic weight (Fe, Cr and Ti) in the alloy. Figure 4a, with low magnification, showed that even though the coatings presented different thicknesses, all of them were homogeneous, and no intact powder particles could be observed. It proved that the impact of the particles on the substrate was efficient at obtaining the deformation of the powder particles and subsequent adhesion layer-by-layer. The exception was coating 3, where the poor layer adhesion was revealed by the presence of cracks, which was a consequence of the lowest particles' velocity (588 m/s). According to the literature, there is a critical velocity of the powder particles where the deposition on the substrate occurs. When the particles' velocity is lower than this critical velocity, the powder particles are rebounded while, when even higher, the powder particles only cause erosion on the substrate; for both cases, there is no material deposition [6,31]. For all coatings, the phases present and their distribution seemed very much the same. From images of high magnification (Figure 4b), the composite microstructure was clearly exhibited with brighter and dispersed equiaxed phases of different sizes and shapes that were well embedded into a darker Al-matrix. From these images, three main areas could be distinguished in the coatings' microstructure, 1- an Al-solid solution matrix, 2- an Al-matrix rich in i-phase (light gray, near-spherical morphology), and 3- an Al-matrix rich in a close to flower-like morphology phase (light gray contrast). As reported by the literature, a spherical morphology is one of the main characteristics of the QC phase, yet the QC phases' approximants, such as $Al_{13}(Cr, Fe)_{2,4,}$ normally lose their spherical feature during solid transformations. The $Al_{13}(Cr, Fe)_{2,4}$ phase is known as a phase that is precedent of the full flower-like phase common in Al-Cr-Fe-X systems [32,33]. The coatings' microstructure was very similar to that of the powder feedstock's microstructure (Figure 1b). The bright features varied significantly in scale, shape, and distribution from location to location within the analyzed areas (Figure 4b). The reason for this was that the feedstock powder's microstructure depended on the particle size, and because the deposition of powders of different sizes took place randomly, the result was a cold-sprayed coating with a composite microstructure.

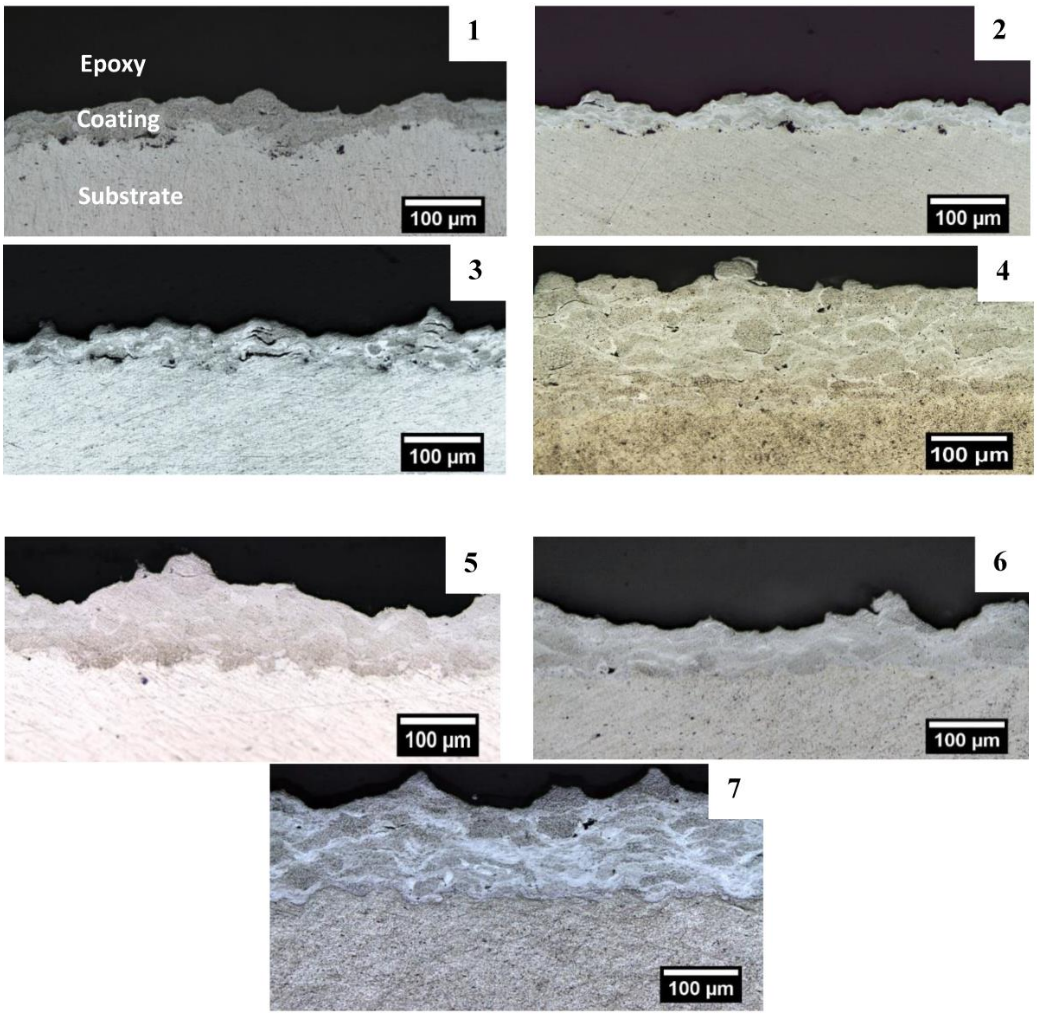

Figure 3. Representative cross-section images taken by Optical Microscopy (OM) showing the coatings' overview and their porosity and thickness when produced using different process parameters.

Figure 5 shows, in higher magnification, such variations in the shape, scale, and distribution of the bright features, even when a small area was considered for the investigation. This was consistent with our previous observations that the size and distribution of quasicrystalline phases varied from particle to particle in the powder [30]. Most of the dispersed phases showed a spherical or nearly spherical shape which indicated the presence of quasicrystalline phases or even their approximants phases after the processing condition. The decomposition of the metastable quasicrystalline phase or its approximant θ: ($Al_{13}(Cr,Fe)_{2,4}$) phase into their corresponding stable crystalline phases was one concern in the processing of Al-Fe-Cr-Ti alloys once the gas heat and/or adiabatic heating upon the particle impacted could favor the decomposition process.

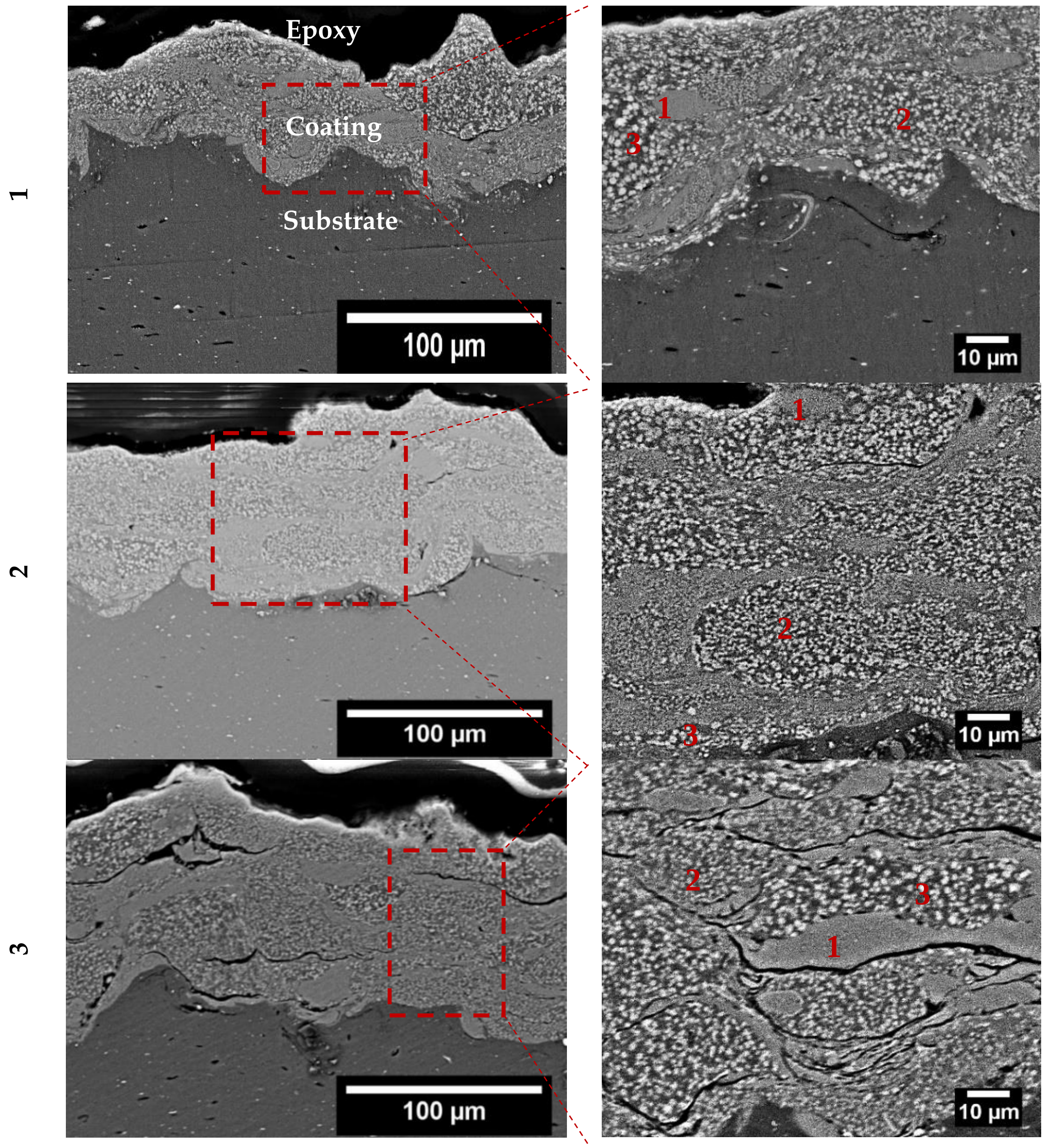

Figure 4. *Cont.*

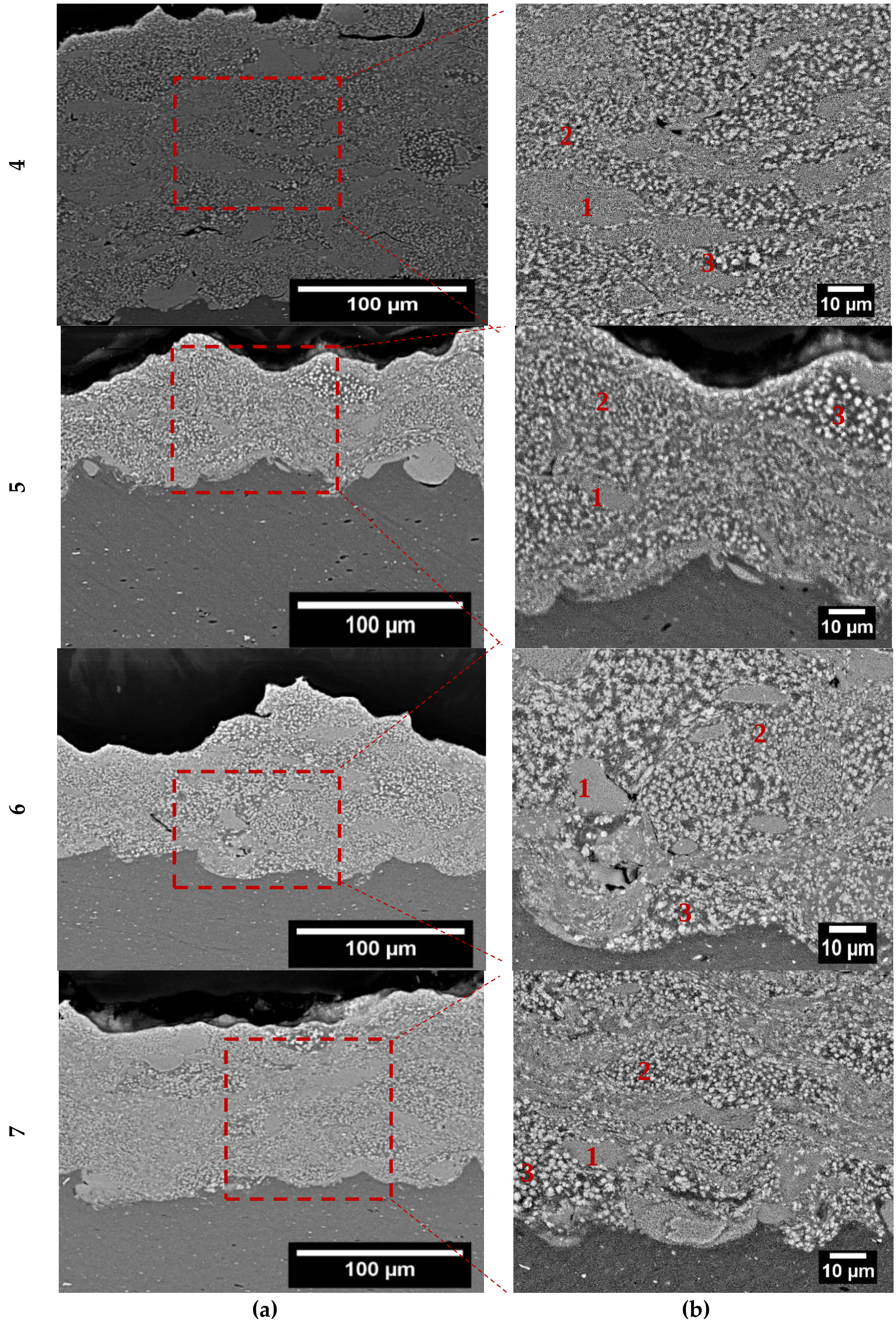

Figure 4. Cross-section images taken by SEM (BSE mode) (**a**) Overview showing the uniformity of the cold-sprayed coatings, (**b**) Details showing a variation in the size and distribution of the dispersoids in the cold-sprayed coatings as obtained using different processing parameters.

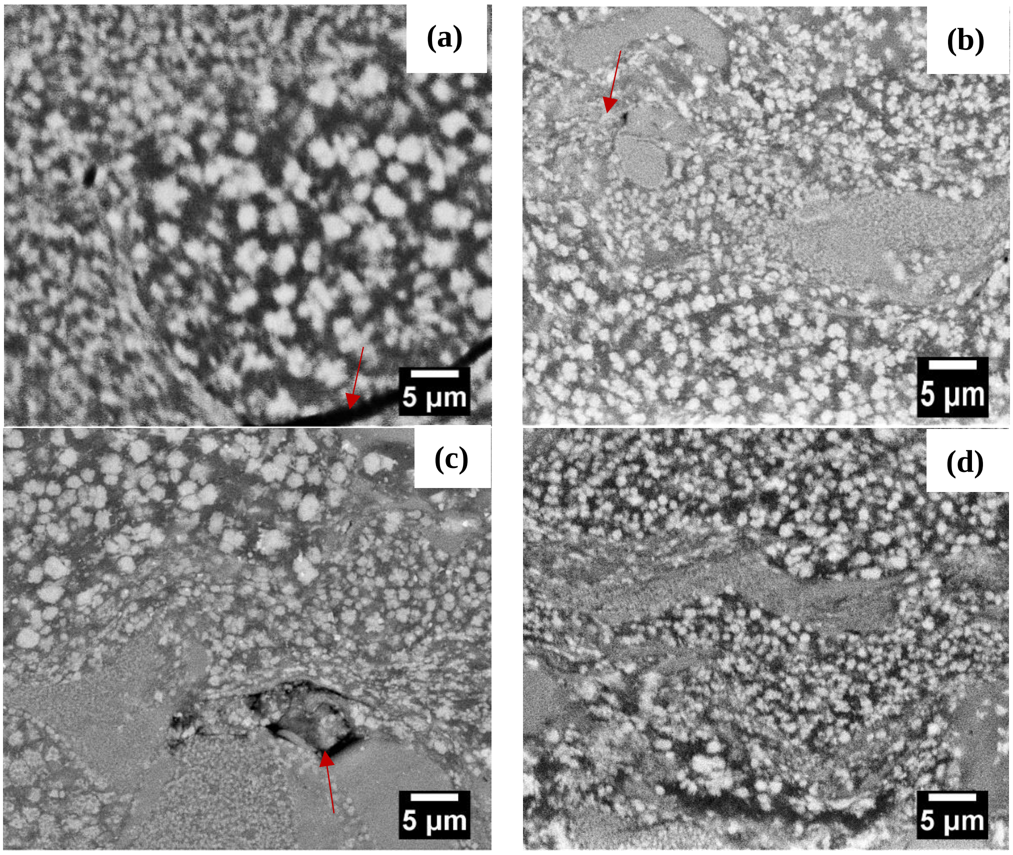

Figure 5. SEM (BSE mode) image of the cross-section showing in high magnification how the bright features varied in shape, scale, and distribution even in the small-analyzed area of the cold-sprayed coating (herein for (**a**) coating 4, (**b**) coating 5, (**c**) coating 6, (**d**) coating 7). Red arrows indicate porosities.

The chemical composition of the coatings and the gas-atomized feedstock powder was evaluated by EDS, and the results are shown in Table 3. From Table 3, there was no significant difference in the chemical composition of the coatings produced using different process parameters. However, when these values were compared with the chemical composition of the feedstock powder, one could see a slight increase in Fe in the coatings. Since there was no obvious reason for such a Fe increase, and considering the standard deviation of the measures, these values were still very close. It is important to mention that the studied alloy was produced using recycled aluminum (Al cans), as detailed in our previous study [30]. As a consequence, the presence of other elements as impurities was expected and could unbalance the alloy's nominal composition $Al_{93}Fe_3Cr_2Ti_2$ (at.%).

Table 3. Chemical composition (at.%) for the gas-atomized powder and cold-sprayed coatings using different process parameters obtained by EDS.

Coating ID	Al	Fe	Cr	Ti
1	91.9 ± 0.1	4.0 ± 0.1	2.2 ± 0.1	2.0 ± 0.1
2	91.4 ± 0.1	4.3 ± 0.1	2.4 ± 0.1	1.9 ± 0.1
3	91.8 ± 0.1	4.0 ± 0.1	2.2 ± 0.1	1.9 ± 0.1
4	91.8 ± 0.1	4.0 ± 0.1	2.3 ± 0.1	1.9 ± 0.1
5	91.8 ± 0.2	4.1 ± 0.1	2.2 ± 0.1	1.9 ± 0.1
6	91.5 ± 0.1	4.2 ± 0.1	2.3 ± 0.1	2.0 ± 0.1
7	91.5 ± 0.1	4.2 ± 0.1	2.3 ± 0.1	2.0 ± 0.1
Powder	92.0 ± 1.3	3.2 ± 0.5	2.0 ± 0.4	2.0 ± 0.2

To prove the presence of the quasicrystalline phase in the cold-sprayed coatings, XRD DSC and TEM analyses were used in combination. Figure 6 shows the XRD patterns from the powder feedstock and the cold-sprayed coatings produced using different processing parameters. The XRD data confirmed the mixture of three main phases α-Al, the i-phase (icosahedral quasicrystalline phase), and ω (Al_3Ti), in the powder feedstock and also in the cold-sprayed coatings. The approximant θ ($Al_{13}(Cr,Fe)_{2\text{-}4}$) phase was also suggested by XRD coatings' data, but mainly for those with particles at higher velocities (coatings 4, 5, 6, and 7). This was due to the partial decomposition of the i-phase into the θ approximant phase. According to the literature [18,34,35], the θ ($Al_{13}(Cr,Fe)_{2\text{-}4}$) phase had an undetermined chemical composition with a distorted monoclinic crystal structure, which presented as its main characteristics of hardness and brittleness and was similar to those of the i-phase [29,35]. Further confirmations of the presence of the i-phase were obtained by DSC analyses.

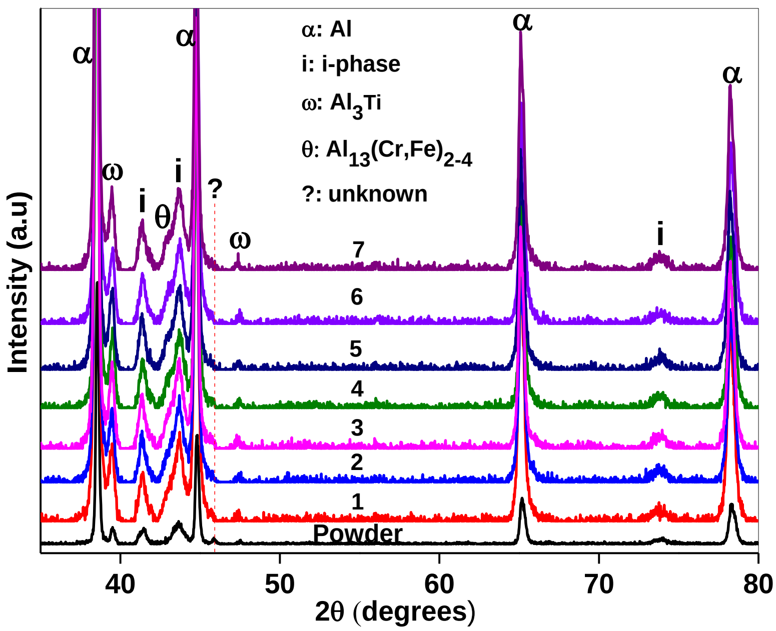

Figure 6. XRD patterns obtained from the gas-atomized feedstock powder and the cold-sprayed coatings produced using different process parameters.

Figure 7 shows the DSC curves of the cold-sprayed coatings that were produced using different processing parameters and the gas-atomized powder feedstock in different size ranges. For comparison, the that was substrate used to produce the coatings was also analyzed in the same conditions. Considering the first heating cycle, all coatings presented a broad exothermic event that could be related to the decomposition of the i-phase and/or its θ approximant phase (Figure 7a). The onset temperature was about 325 °C for all coatings, except for coating 7, which was about 300 °C. By contrast, the offset temperature was around 520 °C for all coatings. Due to the wide range of temperature for such a decomposition, this event count also be observed as two peaks: the first at ~400 °C and the second at ~470 °C. One of them could be related to the decomposition of the θ approximant i-phase ($Al_{13}(Cr,Fe)_{2,4}$). Such an approximant phase could also have a metastable nature and then be decomposed at a different temperature [12,34]. Furthermore, from Figure 7a, the exothermic event was no longer present on the second DSC heating cycle, proving the metastability of the phases. Because of the high thermal stability of metastable phases when combined with the unfavorable thermal kinetics of the cold spray process, no process parameter combination was able to fully decompose the i-phase and/or its θ approximant phase. This shows the advantages of using cold spray to successfully produce coatings of the metastable phase while maintaining their good mechanical properties.

The amount of heat released for each coating, at each temperature, could not be directly compared once the analyzed specimens contained less or more than the i-phase and/or its θ approximant phase depending on location to location, even within the same area of the coating. This could be explained due to the different amounts of the quasicrystalline i-phase and/or its θ approximant phase in the powder feedstock, which depended on the particle size (see Figure 7b) and the conditions to which the feedstock powder was exposed during the coating production. From Figure 7b, the heat released in the metastable i-phase transformation (first heating cycle) decreased with increasing particle size; this was higher for the range of powder particles with a smaller size (<32 μm). Other authors have reported the same observation [36]. Additionally, because the feedstock powder was not submitted to any pressure or heating, it presented the two exothermic events at higher temperatures (~450 °C and ~560 °C) compared to the coatings' peak temperatures. As mentioned before, the amount of the i-phase and θ approximant i-phase could be different from coating sample to coating sample; consequently, the amount of heat released at each temperature could vary from coating to coating.

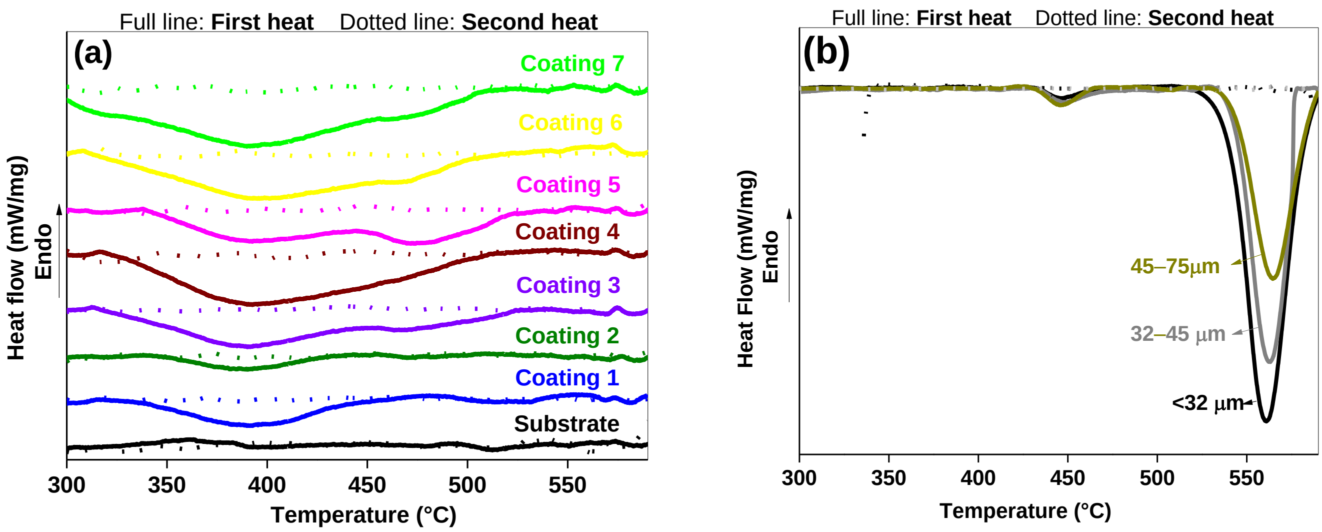

Figure 7. DSC results for (**a**) Cold-sprayed coatings produced using different processing parameters and (**b**) Gas-atomized powder in different size ranges. First heating curves (full lines) and second heating curves (dotted lines).

Figure 8a is a bright-field (BF) TEM image of a region containing particles ≈ 500 nm in diameter (darker gray contrast) embedded into an α-Al matrix (lighter contrast). Here, it is important to mention that Figure 8a is a representative micrograph, and, as mentioned before, the i-phase particles varied in size from area to area within the coating; however, for the other analyzed areas, similar features could be observed. Figure 8b was a selected area diffraction pattern (SADP) that was obtained from the particle marked "X" in Figure 8a. This SADP displays the characteristic five-fold symmetry expected for the [000001] zone axis of the i-phase [19,37–41]. Thus, the bright particles observed in BSE SEM images, such as Figure 4b, were mostly retained in the i-phase. Energy Dispersive X-Ray (EDX) maps (Figure 8c–f) were taken from the selected area in the red dotted square (see Figure 8a) to prove that the i-phase was rich in the alloying elements Al, Fe, and Cr. The EDX point analyses showed a mean chemical composition of $Al_{86.37\pm0.97}Fe_{9.20\pm1.25}Cr_{3.79\pm1.26}Ti_{0.62\pm0.26}$ (at.%), while the Al-matrix expressed $Al_{98.92\pm0.45}Fe_{0.34\pm0.04}Cr_{0.39\pm0.03}Ti_{0.33\pm0.03}$ (at.%). This proved the composite microstructure of a ductile Al-rich matrix with hard i-phase particles dispersed.

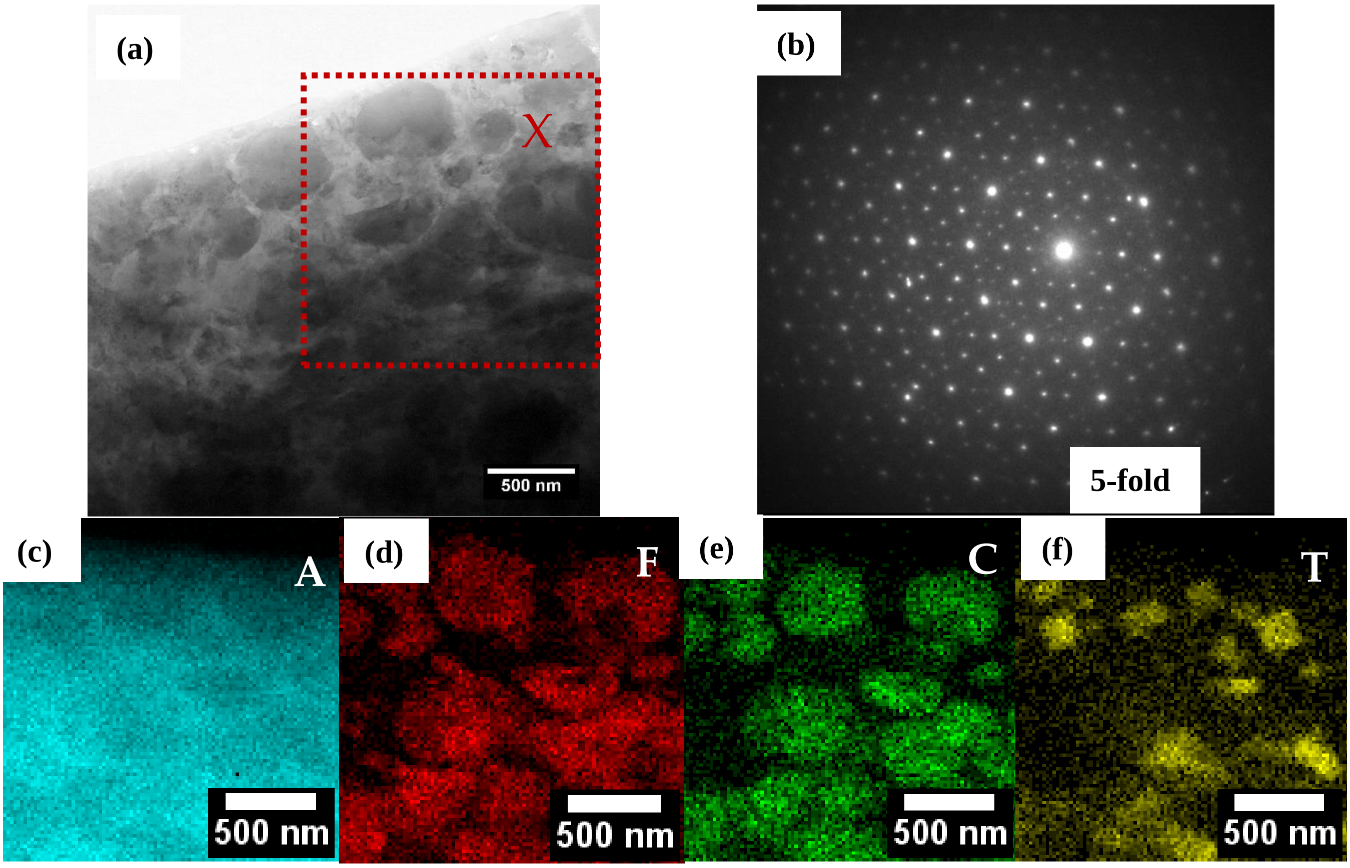

Figure 8. (**a**) Bright-field TEM image from a specimen of coating 4. Lighter contrast: α-Al grains, and darker gray contrast: i-phase particles; (**b**) SADP from the particle marked X in image (**a**), and the elemental EDX maps of the selected area in the red dotted square in (**a**) using (**c**) Al-K, (**d**) Fe-K, (**e**) Cr-K, and (**f**) Ti-K.

3.3. Vickers Microhardness Analyses

Table 4 lists the microhardness of the cold-sprayed coatings produced using different processing parameters. The mean microhardness values were obtained from 18 indentations in each coating, and they varied from 251.9 to 278.9 HV. Considering these high standard deviation values, there was no significant difference in the measures among the coatings. This corroborates with the SEM and XRD results, confirming that similar microstructures present a similar microhardness. These high microhardness values were attributed to the microstructure composed of an α-Al solid solution, the fine grain size, and the i-phase strengthening effect, as well as the approximant θ phase. Due to the non-conventional arrangement of these atoms in the quasicrystalline structure, the i-QC phase was very hard [42,43]. Additionally, the i-QC approximant metastable θ-$Al_{13}(Cr,Fe)_{2,4}$ phase presented with a distorted monoclinic crystal structure, which resulted in high hardness as well [18,29,35]. Thus, combining the ductility of the α-Al matrix with the high hardness of the i-QC phase and its approximant phase, the resulting composites were generally of high strength and balanced ductility [14]. In addition, the low thermal diffusivity of Fe, Cr, and Ti in aluminum allowed the composite microstructure of Al-Fe-Cr-Ti alloys to achieve high strength and good thermal stability at high temperatures, as has been reported [44]. For the studied coatings, the composite microstructure was formed during the gas atomization of the powder feedstock and was maintained in the cold-sprayed coatings. Further, the high standard deviations presented in Table 4 could be explained due to the local variation in the i-phase and/or approximant phases even within the same area, as can be seen from the SEM images (Figure 4). When the indentation was performed in areas rich in the i-phase and/or approximant phases, the microhardness was higher than in any other area. One could note that microhardness values in the range of 200 to 320 HV were obtained for SLMed bulk parts produced from this alloy powder [30], depending on the SLM process parameters. This shows that equivalent hardness could be obtained when the alloy was consolidated by the SLM or CS process from the same powder.

Table 4. Vickers microhardness obtained from the cross-section of the cold-sprayed coatings produced using different process parameters.

Coating ID	Microhardness (HV)
1	277.9 ± 39.3
2	266.4 ± 49.2
3	254.6 ± 24.2
4	271.9 ± 36.0
5	278.9 ± 43.4
6	270.4 ± 40.7
7	251.9 ± 46.0

4. Conclusions

In this work, the quasicrystalline $Al_{93}Fe_3Cr_2Ti_2$ alloy powder was used to produce coatings by cold spray processing using different parameters. The effects of these processing parameters on porosity, adherence, thickness, roughness, microstructure and the Vickers microhardness of the cold-sprayed coatings were investigated. The results obtained are summarized as follows:

(1) The cold-sprayed coatings produced onto unblasted Al-6061 substrates presented lower porosity ($\leq$0.50%), better adherence, and greater thickness. Among these, coating 4 was produced with the highest pressure (4.8 MPa), highest temperature (475 °C), and lower nozzle aperture (A), presenting the greatest thickness (185 µm). The coatings' surface roughness was similar for all coatings.

(2) The coatings produced here exhibited a composite microstructure with the same combination of phases as the feedstock powder, specifically an α-Al with the i-QC phase (icosahedral quasicrystalline phase) and ω phase embedded. A low amount of the approximant θ ($Al_{13}(Cr,Fe)_{2\text{-}4}$) phase was suggested for the coatings, especially those produced with particles at higher velocities (coatings 4, 5, 6, and 7).

(3) The presence of the i-phase was confirmed by XRD; its metastability was proved by DSC, and its icosahedral nature was determined by TEM analyses.

(4) The composite microstructure of the cold-sprayed coatings consisted of a ductile α-Al matrix with an i-QC phase and its approximant θ-$Al_{13}(Cr,Fe)_{2,4}$ phase was embedded. Such a microstructure resulted in coatings with high Vickers microhardness with a mean of about 267 HV and a mean deviation of 8 HV.

(5) The generated results and the knowledge related to the integrity of the parts, microstructure, and achieved mechanical properties allowed the scientific community a better understanding of the quasicrystalline $Al_{93}Fe_3Cr_2Ti_2$ alloy, and its mechanical behavior when obtained by the CSAM route. Additionally, the generated data were helpful to the industrial sector since the results showed the potential of a non-commercial aluminum alloy being applicable.

Author Contributions: A.P.M.d.A.: Conceptualization, Methodology, Formal analysis, Investigation, Writing—original draft, Writing—Review and Editing. F.B.D.M.C.: Data processing and interpretation. E.M.R.: TEM analyses and Writing—Review and Editing. C.S.K.: Resources, Project administration, Funding acquisition, Writing—Review and Editing. P.G.: Conceptualization, Resources, Writing—Review and Editing, Supervision, Project administration, Funding acquisition. All authors have read and agreed to the published version of the manuscript.

Funding: The authors are grateful for the financial support of FAPESP (São Paulo Research Foundation) through projects n. 2013/05987-8, 2017/27031-4, and 2018/04209-5. This study was financed in part by the Coordenação de Aperfeiçoamento de Pessoal de Nível Superior—Brasil (CAPES)—Finance Code 001.

Informed Consent Statement: Not applicable.

Data Availability Statement: The data presented in this study are available on request from the corresponding author.

Acknowledgments: The authors would also like to thank the Structural Characterization Laboratory (LCE) of DEMa/UFSCar for the XRD and TEM analyses, and the Polycontrols Technologies corporation for the fabrication of the cold-sprayed coatings.

Conflicts of Interest: The authors declare no conflict of interest.

References

1. Kim, Y.-K.; Lee, K.-A. Effect of carrier gas species on the microstructure and compressive deformation behaviors of ultra-strong pure copper manufactured by cold spray additive manufacturing. *J. Mater. Sci. Technol.* **2022**, *97*, 264–271. [CrossRef]
2. Prasad, K.; Khalik, M.; Hutasoit, N.; Rashid, R.A.R.; Duguid, A.; Palanisamy, S. Printability of low-cost pre-heat-treated ball milled Al7075 powders using compressed air assisted cold spray additive manufacturing. *Addit. Manuf. Lett.* **2022**, *3*, 100046. [CrossRef]
3. Prashar, G.; Vasudev, H. A comprehensive review on sustainable cold spray additive manufacturing: State of the art, challenges and future challenges. *J. Clean. Prod.* **2021**, *310*, 127606. [CrossRef]
4. Ren, Y.; Tariq, N.U.H.; Liu, H.; Zhao, L.; Cui, X.; Shen, Y.; Wang, J.; Xiong, T. Study of microstructural and mechanical anisotropy of 7075 Al deposits fabricated by cold spray additive manufacturing. *Mater. Des.* **2021**, *212*, 110271. [CrossRef]
5. Kim, Y.-K.; Kim, H.-J.; Lee, K.-A. Solid-state cold spray additive manufacturing of pure tantalum with extraordinary high-temperature mechanical properties. *J. Mater. Res. Technol.* **2023**, *23*, 5698–5709. [CrossRef]
6. Vaz, R.F.; Garfias, A.; Albaladejo, V.; Sanchez, J.; Cano, I.G. A Review of Advances in Cold Spray Additive Manufacturing. *Coatings* **2023**, *13*, 267. [CrossRef]
7. Hutasoit, N.; Javed, M.A.; Rashid, R.A.R.; Wade, S.; Palanisamy, S. Effects of build orientation and heat treatment on microstructure, mechanical and corrosion properties of Al6061 aluminium parts built by cold spray additive manufacturing process. *Int. J. Mech. Sci.* **2021**, *204*, 106526. [CrossRef]
8. Tsaknopoulos, K.; Sousa, B.; Massar, C.; Grubbs, J.; Siopis, M.; Cote, D. A Through-Process Experimental Approach to Enable Optimization of Cold Sprayed Al 7075 Consolidation Performance. *JOM* **2022**, *74*, 249–259. [CrossRef]
9. Sabard, A.; McNutt, P.; Begg, H.; Hussain, T. Cold spray deposition of solution heat treated, artificially aged and naturally aged Al 7075 powder. *Surf. Coat. Technol.* **2020**, *385*, 125367. [CrossRef]
10. Audebert, F.; Prima, F.; Galano, M.; Tomut, M.; Warren, P.J.; Stone, I.C.; Cantor, B. Structural Characterisation and Mechanical Properties of Nanocomposite Al-based Alloys. *Mater. Trans.* **2002**, *43*, 2017–2025. [CrossRef]
11. Saida, J.; Inoue, A. Nanoicosahedral Quasicrystal. In *Encyclopedia of Nanoscience and Nanotechnology*; Nalwa, H.S., Ed.; American Scientific Publishers: Stevenson Ranch, CA, USA, 2004; pp. 795–813.
12. Galano, M.; Audebert, F.; Cantor, B.; Stone, I. Structural characterisation and stability of new nanoquasicrystalline Al-based alloys. *Mater. Sci. Eng. A* **2004**, *375–377*, 1206–1211. [CrossRef]
13. Kang, N.; Fu, Y.; Coddet, P.; Guelorget, B.; Liao, H.; Coddet, C. On the microstructure, hardness and wear behavior of Al-Fe-Cr quasicrystal reinforced Al matrix composite prepared by selective laser melting. *Mater. Des.* **2017**, *132*, 105–111. [CrossRef]
14. Inoue, A. Amorphous, nanoquasicrystalline and nanocrystalline alloys in Al-based systems. *Prog. Mater. Sci.* **1998**, *43*, 365–520. [CrossRef]
15. Inoue, A.; Kimura, H. High elevated-temperature strength of Al-based nanoquasicrystalline alloys. *Nanostruct. Mater.* **1999**, *11*, 221–231. [CrossRef]
16. Wolf, W.; Coury, F.; Kaufman, M.; Bolfarini, C.; Kiminami, C.; Botta, W. The formation of quasicrystals in Al-Cu-Fe-(M=Cr,Ni) melt-spun ribbons. *J. Alloys Compd.* **2018**, *731*, 1288–1294. [CrossRef]
17. Chlupova, A.; Chlup, Z.; Kruml, T. Fatigue properties and microstructure of quasicrystalline AlFeCrTi alloy. *Int. J. Fatigue* **2016**, *91*, 251–256. [CrossRef]
18. Pedrazzini, S.; Galano, M.; Audebert, F.; Collins, D.; Hofmann, F.; Abbey, B.; Korsunsky, A.; Lieblich, M.; Escorial, A.G.; Smith, G. Strengthening mechanisms in an Al-Fe-Cr-Ti nano-quasicrystalline alloy and composites. *Mater. Sci. Eng. A* **2016**, *672*, 175–183. [CrossRef]
19. Kim, K.; Xu, W.; Tomut, M.; Stoica, M.; Calin, M.; Yi, S.; Lee, W.; Eckert, J. Formation of icosahedral phase in an $Al_{93}Fe_3Cr_2Ti_2$ bulk alloy. *J. Alloys Compd.* **2007**, *436*, L1–L4. [CrossRef]
20. Gargarella, P.; Almeida, A.; Vilar, R.; Afonso, C.; Rios, C.; Bolfarini, C.; Botta, W.; Kiminami, C.; Gargarella, P.; Almeida, A.; et al. Microstructural characterization of a laser remelted coating of $Al_{91}Fe_4Cr_3Ti_2$ quasicrystalline alloy. *Scr. Mater.* **2009**, *61*, 709–712. [CrossRef]

21. Stan-Głowińska, K.; Lityńska-Dobrzyńska, L. Influence of Fe addition on the formation of a quasicrystalline phase in bulk Al-rich Al Mn base alloys. *Mater. Charact.* **2017**, *128*, 203–208. [CrossRef]
22. Gargarella, P.; Vilar, R.; Almeida, A.; Kiminami, C.; Rios, C.; Bolfarini, C.; Botta, W. Laser remelting of $Al_{91}Fe_4Cr_3Ti_2$ quasicrystalline phase former alloy. *J. Alloys Compd.* **2010**, *495*, 646–649. [CrossRef]
23. De Araujo, A.P.M.; Micheloti, L.; Kiminami, C.S.; Gargarella, P. Microstructure, phase formation and properties of rapid solidified Al–Fe–Cr–Ti alloys. *Mater. Sci. Technol.* **2020**, *36*, 1205–1214. [CrossRef]
24. García-Escorial, A.; Lieblich, M. Atomization of Al-rich alloys: Three paradigmatic case studies. *J. Alloys Compd.* **2018**, *762*, 203–208. [CrossRef]
25. Dám, K.; Vojtěch, D.; Průša, F. Powder metallurgy Al–6Cr–2Fe–1Ti alloy prepared by melt atomisation and hot ultra-high pressure compaction. *Mater. Sci. Eng. A* **2013**, *560*, 705–710. [CrossRef]
26. Vojtěch, D.; Michalcová, A.; Průša, F.; Dám, K.; Šedá, P. Properties of the thermally stable $Al_{95}Cr_{3.1}Fe_{1.1}Ti_{0.8}$ alloy prepared by cold-compression at ultra-high pressure and by hot-extrusion. *Mater. Charact.* **2012**, *66*, 83–92. [CrossRef]
27. Watson, T.; Nardi, A.; Ernst, A.; Cernatescu, I.; Bedard, B.; Aindow, M. Cold spray deposition of an icosahedral-phase-strengthened aluminum alloy coating. *Surf. Coat. Technol.* **2017**, *324*, 57–63. [CrossRef]
28. Galano, M.; Audebert, F.; Escorial, A.G.; Stone, I.; Cantor, B. Nanoquasicrystalline Al–Fe–Cr-based alloys. Part II. Mechanical properties. *Acta Mater.* **2009**, *57*, 5120–5130. [CrossRef]
29. Liotti, E.; Kirk, C.; Todd, I.; Knight, K.; Hogg, S. Synchrotron X-ray and neutron investigation of the structure and thermal expansion of the monoclinic $Al_{13}Cr_2$ phase. *J. Alloys Compd.* **2019**, *781*, 1198–1208. [CrossRef]
30. de Araujo, A.P.; Kiminami, C.S.; Uhlenwinkel, V.; Gargarella, P. Processability of recycled quasicrystalline Al-Fe-Cr-Ti composites by selective laser melting—A statistical approach. *Materialia* **2022**, *22*, 101377. [CrossRef]
31. Klinkov, S.V.; Kosarev, V.F.; Rein, M. Cold spray deposition: Significance of particle impact phenomena. *Aerosp. Sci. Technol.* **2005**, *9*, 582–591. [CrossRef]
32. Audebert, F.; Galano, M.; Rios, C.T.; Kasama, H.; Peres, M.; Kiminami, C.; Botta, W.; Bolfarini, C. Nanoquasicrystalline Al–Fe–Cr–Nb alloys produced by powder metallurgy. *J. Alloys Compd.* **2013**, *577*, 650–657. [CrossRef]
33. Khoruzha, V.G.; Kornienko, K.E.; Pavlyuchkov, D.V.; Grushko, B.; Velikanova, T.Y. The Al–Cr–Fe phase diagram. I. Phase equilibria at subsolidus temperatures over composition range 58–100 at.% Al. *Powder Metall. Met. Ceram.* **2011**, *50*, 83–97. [CrossRef]
34. Galano, M.; Audebert, F.; Stone, I.; Cantor, B. Nanoquasicrystalline Al–Fe–Cr-based alloys. Part I: Phase transformations. *Acta Mater.* **2009**, *57*, 5107–5119. [CrossRef]
35. Audebert, F.; Colaço, R.; Vilar, R.; Sirkin, H. Laser cladding of aluminium-base quasicrystalline alloys. *Scr. Mater.* **1999**, *40*, 551–557. [CrossRef]
36. Bártová, B.; Vojtěch, D.; Verner, J.; Gemperle, A.; Studnička, V. Structure and properties of rapidly solidified Al–Cr–Fe–Ti–Si powder alloys. *J. Alloys Compd.* **2005**, *387*, 193–200. [CrossRef]
37. Levine, D.; Steinhardt, P.J. Quasicrystals: A New Class of Ordered Structures. *Phys. Rev. Lett.* **1984**, *53*, 2477–2480. [CrossRef]
38. Yamasaki, M.; Nagaishi, Y.; Kawamura, Y. Inhibition of Al grain coarsening by quasicrystalline icosahedral phase in the rapidly solidified powder metallurgy Al–Fe–Ti–Cr alloy. *Scr. Mater.* **2007**, *56*, 785–788. [CrossRef]
39. Li, R.; Dong, Z.; Murugan, V.K.; Zhang, Z.; Khor, K. Microstructure characterization of Al–Cr–Fe quasicrystals sintered using spark plasma sintering. *Mater. Charact.* **2015**, *110*, 264–271. [CrossRef]
40. De Graef, M.; McHenry, M.E. *Structure of Materials: An Introduction to Crystallography, Diffraction and Symmetry*, 2nd ed.; Cam-bridge University Press: Cambridge, UK, 2012. [CrossRef]
41. Elser, V. Indexing problems in quasicrystal diffraction. *Phys. Rev. B* **1985**, *32*, 4892–4898. [CrossRef]
42. Phillips, M.; Thompson, S. The Mechanical Property Data Base from an Air Force/Industry Cooperative Test Program on High Temperature Aluminum Alloys, Wright Lab., Wright-Patterson AFB, OH. Materials Directorate., Ohio 45433-7734, 1994. Available online: https://ntrl.ntis.gov/NTRL/dashboard/searchResults/titleDetail/ADA282911.xhtml (accessed on 9 June 2023).
43. Inoue, A.; Kimura, H.; Yamaura, S.-I. Production and mechanical properties of aluminum alloys with dispersed nanoscale quasicrystalline and amorphous particles. *Met. Mater. Int.* **2003**, *9*, 527–536. [CrossRef]
44. Galano, M.; Audebert, F.; Escorial, A.G.; Stone, I.C.; Cantor, B. Nanoquasicrystalline Al–Fe–Cr-based alloys with high strength at elevated temperature. *J. Alloys Compd.* **2010**, *495*, 372–376. [CrossRef]